Journal of Applied Physics

Characterization of an atmospheric pressure air plasma device under different modes of operation and their impact on the liquid chemistry

Cite as: J. Appl. Phys. **129**, 123303 (2021); https://doi.org/10.1063/5.0039171
Submitted: 30 November 2020 . Accepted: 11 March 2021 . Published Online: 29 March 2021

Sing Wei Ng, Elmar Slikboer, Aaron Dickenson, James L. Walsh, Peng Lu, Daniela Boehm, and Paula Bourke

Journal of Applied Physics ARTICLE scitation.org/journal/jap

Characterization of an atmospheric pressure air plasma device under different modes of operation and their impact on the liquid chemistry

Cite as: J. Appl. Phys. **129**, 123303 (2021); doi: 10.1063/5.0039171
Submitted: 30 November 2020 · Accepted: 11 March 2021 ·
Published Online: 29 March 2021

Sing Wei Ng,[1,2] Elmar Slikboer,[3] Aaron Dickenson,[3] James L. Walsh,[3,a)] Peng Lu,[1,a)] Daniela Boehm,[2] and Paula Bourke[1,2,4,a)]

AFFILIATIONS

[1]Plasma Research Group, School of Biosystems and Food Engineering, University College Dublin, Dublin 4, Ireland
[2]Environmental Sustainability and Health Institute, Technological University Dublin, Dublin 7, Ireland
[3]Department of Electrical Engineering and Electronics, University of Liverpool, Liverpool L69 3BX, United Kingdom
[4]Institute for Global Food Security, School of Biological Sciences, Queens University Belfast, Northern Ireland BT9 5DL, United Kingdom

Note: This paper is part of the Special Topic on: Fundamentals and Applications of Atmospheric Pressure Plasmas.
[a)]**Authors to whom correspondence should be addressed:** J.L.Walsh@liverpool.ac.uk, lvp490@gmail.com, and paula.bourke@ucd.ie

ABSTRACT

It has been shown that plasma generated in contact with liquid can be tailored to tune the composition of plasma functionalized liquids. For biomedical applications, it is necessary to understand the generation of the plasma treated liquids to modulate the composition and thus the biological response. In this work, two distinct discharge compositions were realized by modifying the location of the ground electrode in a pin-to-liquid plasma system. Through this simple modification to the configurations, the spatiotemporal characteristics of the discharge were significantly affected which, in turn, affected the composition of the generated plasma activated water (PAW). Colorimetric testing of the PAW generated from each system revealed that only one configuration was able to generate PAW with a high concentration of H_2O_2. Using time-, space-, and wavelength-resolved imaging of excited plasma species [OH, N_2 (SPS), N_2^+ (FNS), and atomic O], the differences in PAW composition were linked to the differences observed in the discharge dynamics between the two configurations.

I. INTRODUCTION

There has been considerable interest in the interaction between a non-equilibrium atmospheric plasma and a liquid in view of the many potential environmental and biological applications due to their unique ability to generate large concentrations of reactive oxygen and nitrogen species (RONS) in the liquid phase.[1,2] Plasma diagnostics are essential to gain an understanding of the underpinning physical and chemical processes at play, insight that is essential for many applications.[3,4] Electrical measurements, optical emission/absorption spectroscopy, fast imaging, and laser-based approaches are commonly used to study air discharges.[5] Many researchers have employed time-resolved imaging techniques to study the propagation of a plasma discharge.[6–8] Hala *et al.* demonstrated a useful approach in fast imaging of plasma discharges in which optical bandpass filters (BPFs) were used to isolate specific optical emission signals originating from specific excited states in the plasma.[9] In the context of plasma–liquid interaction, it is often reported that several RONS (such as HO•, H_2O_2, HO_2, O_2^-, O_3, NO•, NO_2, HNO_2, HNO_3) will directly interact at the liquid–interface, resulting in a plethora of RONS in the bulk liquid.

There are many different types of plasma–liquid interactions.[10] One type involves generating plasma in the liquid phase. This type of liquid phase plasma emits a high intensity of OH and H_α radicals and can be used for wastewater treatment.[11] Another

type is gas phase plasma with or without direct contact to the liquid. Tsoukou *et al.* generated the plasma activated liquids (PALs) using a dielectric barrier discharge (DBD) with direct contact to different solutions.[12] With DBD direct contact to liquids, they found PALs with differences in concentrations of H_2O_2, NO_2^-, and NO_3^- varied in their antibacterial activity and cytotoxic effects. Traylor *et al.* generated the plasma activated water (PAW) indirectly using a surface DBD installed inside a sealed container.[13] They found that fresh PAW that contains H_2O_2, NO_2^-, and NO_3^- has antibacterial activity.

In this work, we employed a re-configurable air plasma system with direct contact to the liquid that could be tailored to tune the composition of the generated PAW. Several past studies have focused on characterizing the plasma and PAW characteristics from this system, as well as exploring many potential applications.[14–17] These include control of cell cytotoxicity by tuning the composition of the generated PAW.[15] Moreover, fresh cloudy apple juice treated using this system had enhanced quality through the inactivation of the enzyme polyphenol oxidase, and the system has been tuned to mitigate the risk of bovine milk allergens.[16,17]

Despite this wealth of background research, a complete physical understanding of the mechanisms and nature of these discharges created in each configuration was warranted. Notably, PAW generated in one configuration predominantly contains H_2O_2 and NO_3^-, while changing the position of the ground connection results in PAW rich in NO_2^- and NO_3^-.

In this contribution, the chemical composition of PAW generated by both configurations was examined by colorimetric measurement and UV–Vis absorption spectroscopy. To further understand the discharge propagation mechanism in each configuration, time-, space-, and wavelength-resolved imaging was performed. Using narrow bandpass filters at 310, 340, 390, and 780 nm, the emission from excited OH, N_2 (SPS, second positive system), N_2^+ (FNS, first negative system), and atomic O, respectively, were captured. The optical and electrical measurements were used to explain the result of the colorimetric tests and tentatively identify the link between the configuration of the plasma system and the generation of H_2O_2 in the bulk liquid.

II. EXPERIMENTAL SETUP

A. Plasma reactor setup

The electrode setup used in this study comprised of a pin positioned above a liquid volume, two distinct grounding configurations were considered in order to provoke different plasma operating modes; Fig. 1(a) shows "configuration-1" where the liquid volume was directly ground using a metallic rod, and Fig. 1(b) shows "configuration-2" where a grounded electrode was placed beneath a 10 ml liquid volume, providing capacitive coupling to ground through the dielectric container of the liquid. The dual-configuration system used in this investigation was similar to that described in our previous work.[14] A tungsten-copper pin was used as the powered electrode and was placed 5 mm above the surface of de-ionized water contained in a Petri dish.

A 25 kHz sinusoidal high-voltage signal was applied to the pin using a purpose-built power source, to create a discharge between the pin and water surface. The electrical characteristics of the resulting plasma discharge in each configuration was measured via a Tektronix P6015A voltage probe (Radionics Ltd., Ireland) and a Pearson 4100 wideband current monitor (Pearson Electronics Inc., USA). Both the applied voltage and discharge current were recorded on a DSO-X 2014A, Infinii-Vision 2000 X-Series, 4 Channel, 100 MHz, 2 GSPS digital oscilloscope (Radionics Ltd., Ireland). Recorded waveforms for both conditions are shown in Fig. 2, while the electrical operating conditions used for both configurations are summarized in Table I. In both cases, the dissipated power in the system was calculated in real-time from the voltage and current waveforms. The applied voltage was chosen such that the dissipated power was similar in both conditions at the moment of breakdown, approximately 27 W. During plasma generation, it is well known that the conductivity of the liquid changes, resulting in inevitable and unavoidable fluctuation in the dissipated power. The

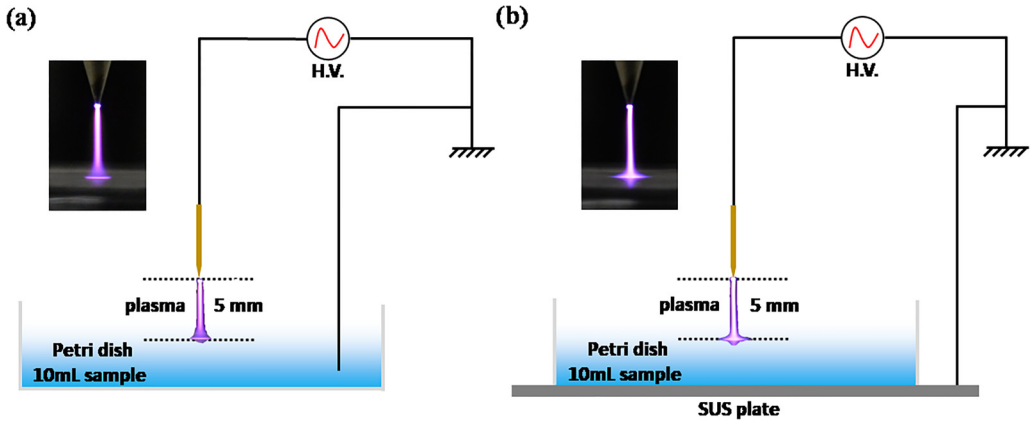

FIG. 1. Schematic of air discharges of (a) configuration-1 and (b) configuration-2 above water.

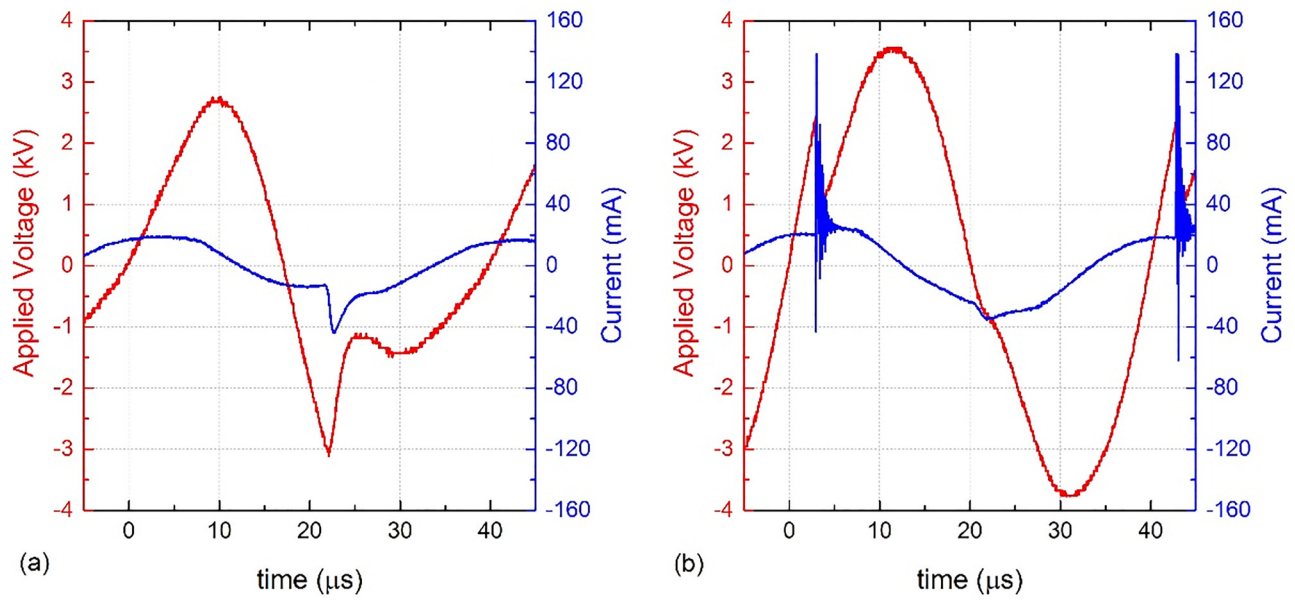

FIG. 2. Voltage–current waveforms for the plasma system in configuration-1 shown in (a) and for configuration-2 in (b).

range of dissipation at a constant voltage, for both configurations, is shown in Table I.

B. Plasma activated water generation

In order to generate PAW for liquid phase chemical analysis, 10 ml of de-ionized water was added to a 5.5 cm internal diameter polystyrene Petri dish (Sarstedt Ltd., Ireland) and exposed to the plasma discharge over a 10 min period.

C. Colorimetric measurement of RONS in PAW

To assess changes in the chemical composition of PAW, a number of colorimetric tests were performed. H_2O_2 concentrations in plasma activated water (PAW) were quantified using titanium oxysulfate ($TiOSO_4$, Sigma-Aldrich, Arklow, Ireland) and spectrophotometric measurements.[14] The calibration curve of known H_2O_2 concentrations (0, 82, 163, 326, 653, 979, and 1632 μM) was prepared by diluting 30% H_2O_2 standard solution (Perhydrol® for analysis EMSURE® ISO) and used to convert absorbance into H_2O_2 concentration. Briefly, 10 μl of $TiOSO_4$ solution and 100 μL of PAW or calibration curve samples were added to a 96-well microtiter plate (Sarstedt Ltd., Ireland). After a reaction time of 10 min at room temperature, the absorbance was read on a spectrophotometric plate reader (Synergy HTX multi-mode microplate reader, BioTek Instruments Inc., Ireland) at 405 nm.

Nitrite concentration was measured using the Griess reagent (Sigma-Aldrich, Arklow, Ireland). A range of known concentrations of sodium nitrite (Sigma-Aldrich, Arklow, Ireland) solutions (0, 20, 40, 60, 80, and 100 μM) were used to prepare an NO_2^- calibration curve and to convert absorbance into NO_2^- concentration. 50 μl of the Griess reagent and 50 μl of PAW or calibration curve samples were added to a 96-well microtiter plate. After a reaction time of 30 min in dark conditions, the absorbance was read at 548 nm.

Nitrate concentration was determined with 2,6-dimethyl phenol (DMP) using the Spectroquant® nitrate assay kit (Merck Chemicals, Darmstadt, Germany) following the manufacturer's instructions with minor modification. Samples were pretreated with sulfamic acid to eliminate the nitrite interference. A set of standard concentrations of sodium nitrate solutions (0, 0.1, 0.25, 0.5, 1, 2.5, and 5 mM) were used to prepare a NO_3^- calibration curve and to convert absorbance into NO_3^- concentrations. Briefly, 200 μl of reagent A, 25 μl of PAW or calibration curve samples, and 25 μl of reagent B was added in order into a 1.5 ml microtube and then mixed vigorously. After a reaction time of 20 min at room temperature, 100 μl of the total mixture was added to a 96-well microtiter plate and the absorbance was read at 340 nm.

TABLE I. Parameters setting for configuration-1 and configuration-2.

Parameters	Configuration-1	Configuration-2
Frequency (kHz)	25	25
Voltage (kV)	5.5	7.5
Power (W)	26–28	25–29

D. UV absorption spectroscopy

To further analyze the changes in liquid chemistry as a result of plasma treatment, UV absorption was considered using a UV–Vis spectrophotometer (Biochrom Libra S22, UK). As confirmed by Girard *et al.*, the absorption spectra of plasma generated RONS

in the liquid phase lie within the UV range (200–400 nm).[18] To perform the absorption measurement, the samples were contained in a quartz cuvette (100-QS, Hellma Analytics, Sigma-Aldrich, Ireland) with a standard optical path of 10 mm. The detection limit of the instrument was 0.001, and the absorption spectra were recorded at room temperature from 200 to 500 nm. The spectral resolution was 1 nm, and the nominal scan speed was 250 nm/min.

To aid in RONS identification, standard solutions were prepared for 1 mM H_2O_2, 1 mM HNO_2, and 5 mM HNO_3 in de-ionized water. HNO_2 was prepared using a $NaNO_2$ and HCl solution as follows:

$$HCl + NaNO_2 \rightarrow NaCl + HNO_2. \quad (1)$$

HNO_3 was prepared using a $NaNO_3$ and HCl solution as follows:

$$HCl + NaNO_3 \rightarrow NaCl + HNO_3. \quad (2)$$

Optical absorbance data of PAW samples were analyzed by comparing the optical absorbance spectra of the standard solutions.

E. Time- and wavelength-resolved discharge imaging

For both configurations, time-resolved imaging of the discharge was performed using an intensified CCD (iCCD) camera (Andor iStar DH734) to resolve the plasma dynamics. Using a kinetic series, the entire plasma period of 40 μs was captured by varying a relative delay using single shot imaging with an exposure time of 500 ns. Additionally, short-exposure iCCD images were taken using several bandpass filters (BPFs) of 310, 340, 390, and 780 nm (Thorlabs, UK) to look at specific optical emission from the plasma. The four BPFs had a bandwidth of 10 nm and were used to capture emission from excited OH (A-X) at approximately 310 nm, N_2 (SPS) at approximately 340 nm, N_2^+ (FNS) at approximately 390 nm, and atomic O at approximately 780 nm. Since less light reached the detector when a BPF was used, the positive half-period and negative half-periods were separately resolved using 20 μs exposures. Each image shown was comprised using an accumulation of 30 exposures.

The full period time-resolved images were analyzed by creating a spatiotemporal graph. This was done by horizontally binning the light emission from each image at each time delay to get an intensity line graph at that time, which in combination with all the other time delays creates a spatiotemporal graph.

III. RESULTS AND DISCUSSION

A. Formation of RONS in the liquid phase

PAW generated by both configurations was analyzed by quantifying the concentration of H_2O_2, NO_2^-, and NO_3^- using colorimetric analysis. It was determined that for configuration-1, shown in Fig. 3(a), the NO_2^- concentration in μmol/l increased logarithmically in time t in min following

$$[NO_2^-] = 67.784 \ln t + 152.23.$$

The NO_3^- concentration of the PAW generated by configuration-1 was found to increase linearly with a slope of 0.1135 mM/min, while measurements revealed that no H_2O_2 was produced. In configuration-2, shown in Fig. 3(b), it was determined that both the H_2O_2 and NO_3^- concentration increased linearly with a slope of 92.43 μM/min and 0.3737 mM/min, respectively. However, no NO_2^- was detected in this configuration. Consequently, it can be summarized that PAW generated by configuration-1 was predominantly composed of NO_2^- and NO_3^-, while PAW from configuration-2 was predominantly composed of H_2O_2 and NO_3^-. These results are in close agreement with our previous works.[14]

To further assess the composition of PAW created in each configuration, its UV absorption spectra was analyzed and compared with that of standard solutions of 1 mM H_2O_2, 1 mM HNO_2, and 5 mM HNO_3. Figure 4 shows the absorbance spectra of PAW and the standard solutions. This figure highlights three main contributions corresponding to the absorbance of H_2O_2 around 260 nm, NO_3^- peaking at 300 nm and NO_2^- in the range of 330–400 nm as

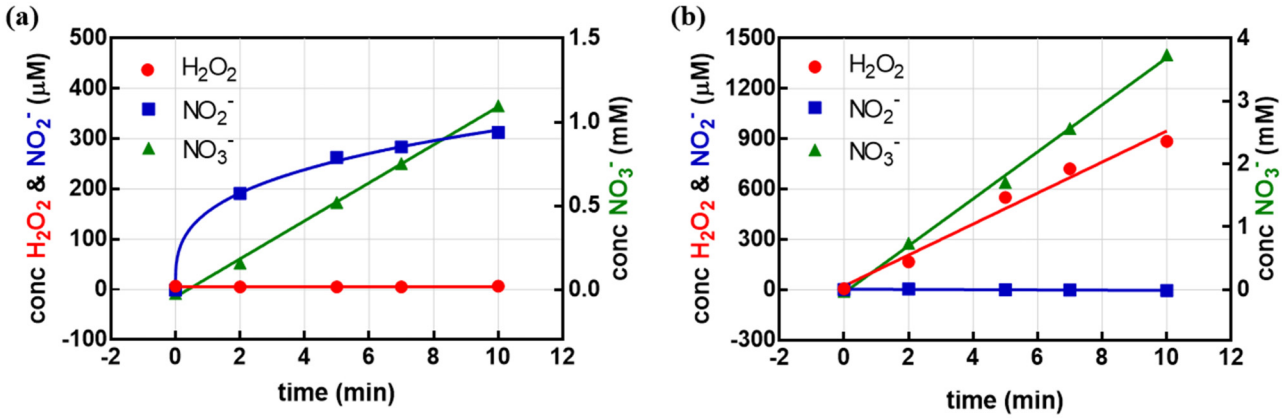

FIG. 3. Concentration plots of H_2O_2, NO_{2-}, and NO_{3-} in plasma activated water (PAW) produced by (a) configuration-1 and (b) configuration-2.

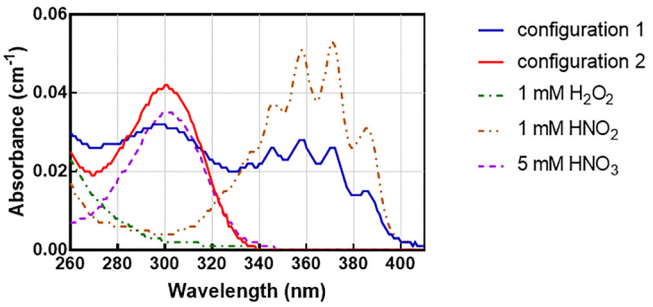

FIG. 4. UV absorbance spectrum of PAW of configuration-1, configuration-2, 1 mM H_2O_2, 1 mM HNO_2, and 5 mM HNO_3.

reported by Brubaker *et al.* and Girard *et al.*[18,19] The spectra of HNO_2 in the range of 330–400 nm observed as five finger-like peaks, while the spectra of $NaNO_2$ or NO_2^- occurred around 350 nm.[19] H_2O_2 in PAW from both configurations was difficult to detect from the UV spectra, because no obvious peak at 260 nm was present in the UV spectra. PAW generated by both configurations was found to contain NO_3^-, evidence by the peak observed at 300 nm. Notably, the distinctive five peaks associated with HNO_2 was only observed in the absorption spectra of PAW created by configuration-1. The PAW created by configuration-2 had an absorption peak at 300 nm, aligning well with the absorption maxima of HNO_3. These results agree well with those obtained by the colorimetric measurements; configuration-1 was found to create substantial quantities of both NO_2^- and NO_3^-, which are both observed in the absorption spectra. In configuration-2, no NO_2^- was detected in the PAW, while no HNO_2 is observed in the absorption spectra.

Critically, RONS play an important role in the field of plasma medicine applications, with H_2O_2 being reported to be involved in the antimicrobial action of PAW.[20,21] Furthermore, Weller and Finnen and Afzali *et al.* reported that the acidified nitrite was able to accelerate wound healing in rats with type 2 diabetic rats.[22,23] It was also reported that acidified nitrite was a novel antimicrobial agent for cutaneous pathogens, such as *Trichophyton mentagrophytes*, *T. rubrum*, *Candida albicans*, *Streptococcus pyogenes*, *Staphylococcus aureus*, and *Propionibacterium acnes*.[24] Naïtali *et al.* proposed that nitrate had antimicrobial effect in the combination of nitrite in the acidic condition.[21] Hence, the ability to manipulate and tune the composition in PAW is of vital importance from an application perspective.

B. Time-resolved discharge imaging

To understand how each electrode configuration yields, a distinct PAW composition time-resolved short-exposure imaging was performed. iCCD imaging for the discharges occurring when the system is in configuration-1 and -2 as shown in Figs. 5(a) and 5(b), respectively. When the system was operated in configuration-1, a single breakdown event in one complete applied voltage period was observed, this occurred in the negative half-period at 22 μs [Fig. 5(a)]. It can be seen that an intense streamer discharge was initiated at the powered pin electrode and propagated toward the liquid surface. As the discharge occurred only in the negative half-period of the applied voltage waveform, the pin electrode was acting as an instantaneous cathode, thus indicating that the streamer is anode directed. The light intensity was found to be the highest when in close proximity to the pin electrode. The intense streamer discharge was only visible for ~1.5 μs, after which an afterglow that was spatially confined to the pin electrode was observed to last for a further 20 μs.

Figure 5(b) shows that the discharge dynamics when the system is operated in configuration-2 differs significantly from that observed in configuration-1. At approximately 3 μs into the positive-half cycle of the applied voltage waveform, when the pin electrode was the instantaneous anode, an intense cathode-directed streamer was observed. Following streamer propagation, a period of afterglow was observed to persist for approximately 10 μs at the water surface. During the negative half-period, a secondary breakdown event was observed at 21 μs. The dynamics of this streamer were very similar to those observed in configuration-1, yet the intensity was approximately 5-fold lower. The afterglow for the negative streamer occurs only at the vicinity of the HV electrode, following a similar pattern to that observed in Fig. 5(a).

C. Wavelength-resolved discharge imaging

Wavelength-resolved imaging was used to gain an appreciation for the generation of excited states within the discharge created by each configuration. Figure 6 shows the accumulated light emission for the positive and negative half-period with the system in configuration-1 and -2 separately. The upper and lower red lines indicate the locations of HV electrode and water surface.

During the positive half-period, there is no emission at any wavelength in configuration-1, matching the results shown in Fig. 5(a). During the negative half-period, emission observed using the BPF of 310 nm [including OH emission and N_2 SPS (0,0) band] reached an intensity of 5×10^3 counts at 1 mm from the liquid surface, and 1×10^4 counts were detected closer to the HV electrode. Critically, the emission from excited OH does not appear to contact with the liquid surface, a finding that may explain the lack of H_2O_2 detected in the liquid phase when using configuration-1, as OH in the gas phase is a precursor of H_2O_2 in

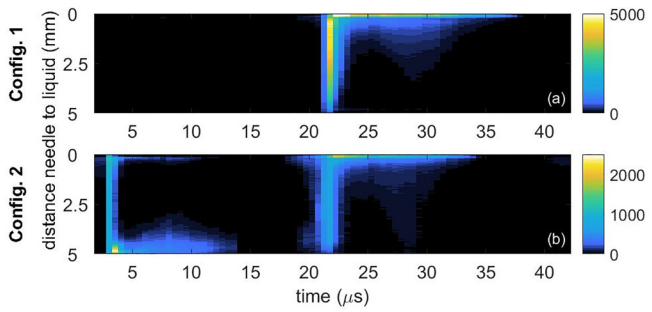

FIG. 5. Time-resolved fast iCCD imaging to resolve the entire plasma period using 500 ns steps when the system is in configuration-1 (a) and -2 (b). The distance is measured from the tip of the needle to the liquid surface.

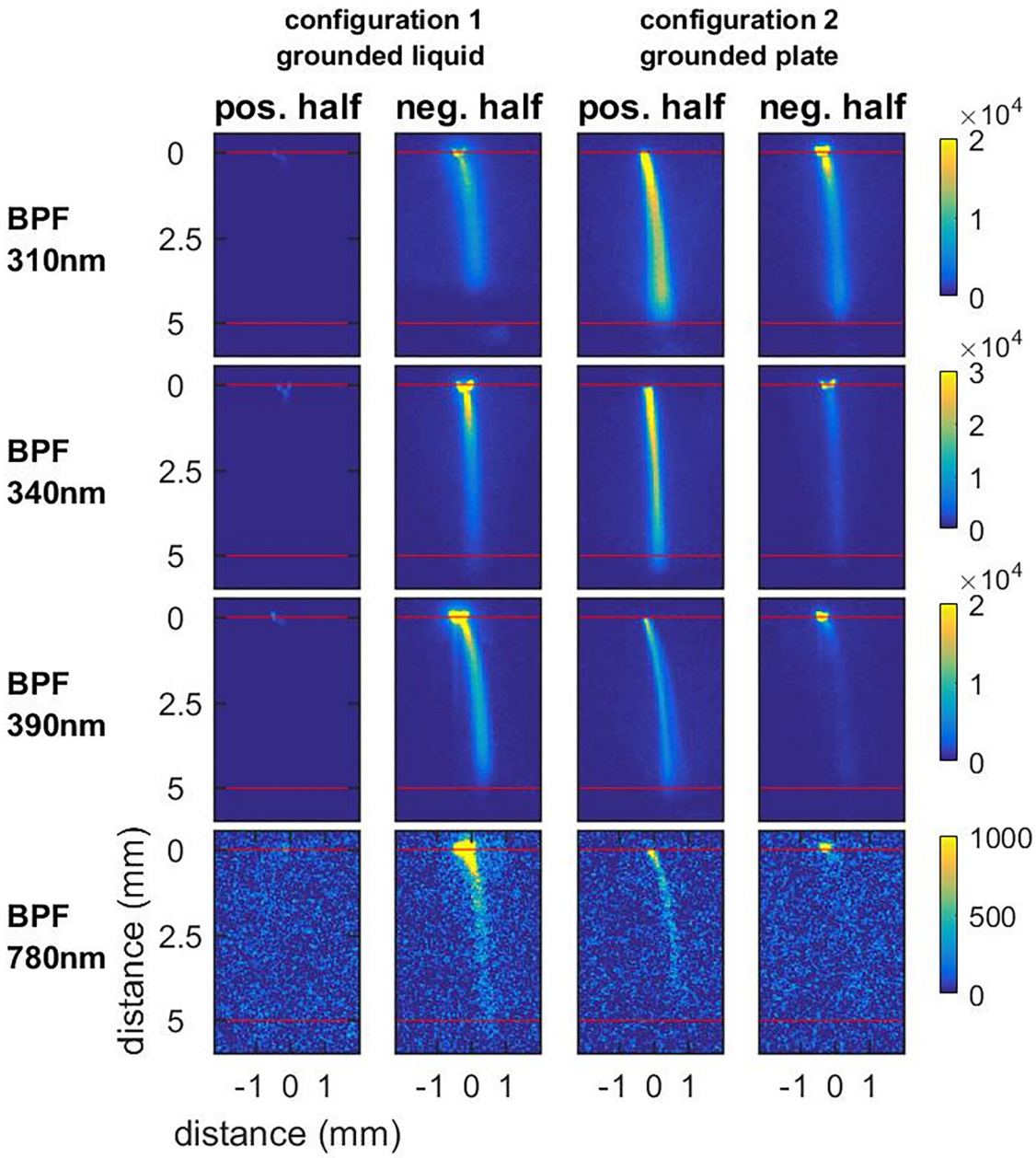

FIG. 6. Species-resolved images of configuration-1 and configuration-2 at positive and negative half-periods through narrow bandpass filters of 310, 340, 390, and 780 nm for emissions from OH, N_2 (SPS), N_2^+ (FNS), and atomic O, respectively. The upper red line indicates the location of the tip of HV needle, while the lower red line indicates the location of the water surface.

the liquid phase.[25] Light emissions at 340 and 390 nm (representing N_2 and N_2^+ emissions) appear to show contact with the liquid, although the intensities are an order of magnitude higher at the electrode (3×10^4 counts), reducing by an order of magnitude away from the electrode. The light emission at 780 nm (atomic O) was very weak throughout the entire discharge.

With the system in configuration-2, the wavelength-resolved emission clearly highlighted the presence of a streamer during the positive half-period of the applied voltage. Emission at 310 nm reached reach a maximum of 2×10^4 counts close to the HV electrode, while still reaching approximately 1×10^4 counts close to the liquid surface. The presence of OH emission in close proximity to

the liquid surface when using this configuration may account for the presence of H_2O_2 in the bulk liquid due to interactions occurring at the liquid interface. The light emission at 340 and 390 nm appeared similar to those observed at 310 nm.

The differences in spatiotemporal profile of the discharges in each configuration clearly lead to a significant variation in the composition of the resultant PAW, most notably in the generation of H_2O_2, which is an important molecule for biological applications. In configuration-1, H_2O_2 was completely absent, which is in stark contrast to that observed in configuration-2, where μM concentrations were measured. We hypothesize that this major difference can be attributed to two key factors: (1) OH emission, which may be used as an indirect indicator of ground-state OH density, does not appear to reach the liquid surface in configuration-1, indicating a reduced concentration of an important precursor for H_2O_2 formation. To support this hypothesis, computational studies of streamers in atmospheric pressure air have shown that the electric field in an anode directed streamer, i.e., the only discharge observed in configuration-1, is considerably weaker than that in a corresponding cathode directed streamer.[26] From this, it may be inferred that a weaker electric field leads to a reduction in the generation of OH and consequently H_2O_2 in the liquid phase. Previous studies have also shown that OH formed in the plasma phase is the primary source of H_2O_2 in the bulk liquid.[25]

It is clear that some OH states have not been detected in optical emission imaging studies. Undetected OH can reach the liquid surface and consequently form H_2O_2 in the liquid phase. In configuration-1, no H_2O_2 was detected in PAW, because only small amounts of OH might be generated above the water surface that reacted with NO, forming NO_2^- and NO_3^-.[14] Second, H_2O_2 in the liquid phase could be electrolyzed and form oxygen bubbles around the grounded electrode.[27]

(2) An afterglow lasting ~10 μs was formed at the liquid surface during the positive half-cycle of the applied voltage waveform in configuration-2, no such afterglow was observed in either half-period when configuration-1 was adopted. In configuration-1, the plasma was observed to briefly interact with the liquid surface for a maximum of 2 μs during the negative half-cycle of the applied voltage cycle. Under such circumstances, it may be assumed that longer-lived chemical species, such as NO, created in the plasma phase diffuse to the liquid surface and significantly influence the liquid chemistry. Conversely, in configuration-2, the plasma had a significantly longer contact time with the liquid, enabling short-lived species, such as O and OH, to take part in reactions at the interface.

IV. CONCLUSIONS

This study advanced the characterization of a pin-to-liquid plasma system operated in two different configurations. In configuration-1, the liquid was directly electrically grounded via a stainless-steel rod, while in configuration-2, a large ground plate was placed beneath the Petri dish reservoir holding the liquid. Even though the grounding is the only external difference to the system, there were significant differences identified in the induced chemistry of the PAW. It was shown that in configuration-1 no H_2O_2 is created in the liquid, with the chemistry being dominated by NO_2^- and NO_3^-. When the system was operated in configuration-2, high concentrations of H_2O_2 and NO_3^- were detected alongside with no NO_2^- measurable.

Space-, time-, and wavelength-resolved imaging of the discharge showed that, when the system operates in configuration-2, there are two discharges for every one applied voltage period. When configuration-1 is adopted, only a single discharge event during the negative half-period was observed.

Ultimately, it can be concluded that the differences in the grounding of the plasma system gave rise to significantly different discharge dynamics, with one configuration producing both anode-directed and cathode-directed streamers, while the other configuration produced only anode-directed streamers. Critically, both systems were capable of generating RONS within a liquid volume, yet the composition of the PAW created was different in each case. In configuration-1, it was observed that only a single, anode-directed streamer was created during each period of the applied voltage, which was assumed to compromise OH and subsequently H_2O_2 production in the liquid.

These results are in good agreement with the results of Nikiforov *et al.* and Xiong *et al.*[28,29] Nikiforov *et al.* found that the density of OH radicals emitted from an anode-directed streamer is almost 2-fold lower than from a cathode-directed streamer.[29] Xiong *et al.* also discovered that a higher OH density was observed during cathode-directed streamer discharge. The higher OH density presented in the cathode-directed streamer can be attributed to the fact that the positive column is constricted by bombarded ions and, therefore, the current density is higher than in the anode-directed streamer, according to those authors.

From an electrical point of view, the interplay between the impedance of the power source and the coupling of the plasma, through the liquid, to ground causes a shift in the dynamics of the discharge which ultimately impacts the chemistry of the generated PAW. To improve the tunability of chemistry in PAW, instead of using a container, using a grounded electrode coated with various dielectric materials with different thicknesses might give additional insight. In addition, to improve the measurement of the dynamics of all states of OH, laser-induced fluorescence will be employed in further studies.

From an application perspective, this is important as it confirms that the composition of PAW can be tailored simply by varying the electrode configuration. Many potential applications of PAW, such as microbial decontamination or immune stimulatory effects, are enhanced by the presence of H_2O_2, thus this work demonstrates a way in which H_2O_2 production in PAW can be significantly enhanced.

ACKNOWLEDGMENTS

This work was supported by a UK Royal Society and Royal Irish Academy cost-share program (No. IEC\R1\180090), with further support from the Science Foundation Ireland (SFI) under the Grant Nos. 16/BBSRC/3391 and 20/US/3678, and the EPSRC under Grant Reference Nos. EP/N021347/1 and EP/R041849/1.

DATA AVAILABILITY

The data that support the findings of this study are available from the corresponding author upon reasonable request.

REFERENCES

[1]M. Laroussi, X. Lu, and C. M. Malott, Plasma Sources Sci. Technol. **12**(1), 53 (2003).
[2]B. Locke, M. Sato, P. Sunka, M. Hoffmann, and J.-S. Chang, Ind. Eng. Chem. Res. **45**(3), 882–905 (2006).
[3]A. F. Gaisin and E. E. Son, High Temp. **48**(3), 447–450 (2010).
[4]P. Mezei, T. Cserfalvi, and L. Csillag, J. Phys. D **38**(16), 2804 (2005).
[5]R. Engeln, B. Klarenaar, and O. Guaitella, Plasma Sources Sci. Technol. **29**(6), 063001 (2020).
[6]J. L. Walsh and M. G. Kong, IEEE Trans. Plasma Science **39**(11), 2306–2307 (2011).
[7]J. Lai and J. E. Foster, J. Phys. D **53**(2), 025206 (2020).
[8]J.-S. Oh, Y. Aranda-Gonzalvo, and J. W. Bradley, J. Phys. D **44**(36), 365202 (2011).
[9]M. Hala, O. Zabeida, B. Baloukas, J. E. Klemberg-Sapieha, and L. Martinu, IEEE Trans. Plasma Sci. **38**(11), 3035–3039 (2010).
[10]S. W. Ng, E. Tsoukou, S. Chaple, D. Boehm, and P. Bourke, *Innovative Food Processing Technologies* (Elsevier, 2021), pp 610–634.
[11]S. Horikoshi and N. Serpone, RSC Adv. **7**(75), 47196–47218 (2017).
[12]E. Tsoukou, P. Bourke, and D. Boehm, Plasma Med. **8**(3) (2018).
[13]M. J. Traylor, M. J. Pavlovich, S. Karim, P. Hait, Y. Sakiyama, D. S. Clark, and D. B. Graves, J. Phys. D **44**(47), 472001 (2011).
[14]P. Lu, D. Boehm, P. Bourke, and P. J. Cullen, Plasma Processes Polym. **14**(8), 1600207 (2017).
[15]P. Lu, D. Boehm, P. Cullen, and P. Bourke, Appl. Phys. Lett. **110**(26), 264102 (2017).
[16]A. E. Illera, S. Chaple, M. T. Sanz, S. Ng, P. Lu, J. Jones, E. Carey, and P. Bourke, Food Chem. **3**, 100049 (2019).
[17]S. W. Ng, P. Lu, A. Rulikowska, D. Boehm, G. O'Neill, and P. Bourke, Food Chem. **342**, 128283 (2020).
[18]F. Girard, V. Badets, S. Blanc, K. Gazeli, L. Marlin, L. Authier, P. Svarnas, N. Sojic, F. Clément, and S. Arbault, RSC Adv. **6**(82), 78457–78467 (2016).
[19]T. R. Brubaker, K. Ishikawa, K. Takeda, J.-S. Oh, H. Kondo, H. Hashizume, H. Tanaka, S. D. Knecht, S. G. Bilén, and M. Hori, J. Appl. Phys. **122**(21), 213301 (2017).
[20]R. Burlica, R. G. Grim, K. Y. Shih, D. Balkwill, and B. R. Locke, Plasma Processes Polym. **7**(8), 640–649 (2010).
[21]M. Naïtali, G. Kamgang-Youbi, J. M. Herry, M. N. Bellon-Fontaine, and J. L. Brisset, Appl. Environ. Microbiol. **76**(22), 7662–7664 (2010).
[22]H. Afzali, M. Khaksari, R. Norouzirad, S. Jeddi, K. Kashfi, and A. Ghasemi, Nitric Oxide **103**, 20–28 (2020).
[23]R. Weller and M. J. Finnen, Nitric Oxide **15**(4), 395–399 (2006).
[24]R. Weller, R. Price, A. Ormerod, N. Benjamin, and C. Leifert, J. Appl. Microbiol. **90**(4), 648–652 (2001).
[25]S. A. Norberg, W. Tian, E. Johnsen, and M. J. Kushner, J. Phys. D **47**(47), 475203 (2014).
[26]A. Luque, V. Ratushnaya, and U. Ebert, J. Phys. D **41**(23), 234005 (2008).
[27]P. Rumbach, M. Witzke, R. M. Sankaran, and D. B. Go, J. Am. Chem. Soc. **135**(44), 16264–16267 (2013).
[28]Q. Xiong, Z. Yang, and P. J. Bruggeman, J. Phys. D **48**(42), 424008 (2015).
[29]A. Nikiforov, Q. Xiong, N. Britun, R. Snyders, X. P. Lu, and C. Leys, Appl. Phys. Express **4**(2), 026102 (2011).